# Control Strategies of Converter-Based Online Impedance Spectroscopy for Photovoltaic Panels

Xin Wang, Zhixue Zheng, Michel Aillerie, Jean-Paul P Sawicki, Alexandre de Bernardinis, Marie-Cécile C Péra, Daniel Hissel

# Control Strategies of Converter-Based Online Impedance Spectroscopy for Photovoltaic Panels

Xin Wang, *Student Member, IEEE,* Zhixue Zheng, *Member, IEEE,* Michel Aillerie, Jean-Paul Sawicki, Alexandre De Bernardinis, *Member, IEEE,* Marie-Cécile Péra, Daniel Hissel, *Fellow, IEEE*

***Abstract*—Impedance spectroscopy (IS) provides a powerful, non-destructive way to acquire photovoltaic (PV) panels' internal impedance over a wide frequency range. Compared with specific workstation-based IS, converter-based IS performed as an added function of the PV power converter provides an attractive mean to achieve online measurements. It can help reduce overall system costs and facilitates online applications, as no additional equipment is required. However, the control strategy of the power converter should be specifically designed. This work aims to provide a systematic design guideline for control strategies of converter-based IS implementation. Meanwhile, a cooperative control scheme between maximum power point tracking (MPPT) and IS modes is proposed to ensure quasi-maximum output power even during IS monitoring mode. For IS mode, two control strategies, named unified control and separated control are designed and compared based on three commonly used compensation controllers in linear system control, i.e., proportional (P), proportional-integral (PI) and quasi-proportional resonant (QPR) controllers. In the unified control strategy, a single PI controller controls the DC and AC components together to meet the control objectives. Meanwhile, in the separated control strategy, a segmented lower pass filter (LPF) with a variable cut-off frequency is designed to effectively separate the DC component of the PV current from the AC perturbation signals. Finally, an experimental study is conducted to verify that under both control strategies, reliable and accurate IS measurements can be achieved. Particularly, the unified control strategy based on a single PI controller is chosen for the cooperative control between MPPT and IS modes considering its control simplicity, high tracking accuracy (i.e., 99.5% and 93.7% for DC and AC components separately) and sufficient signal-to-noise ratio (SNR) (i.e., 6.9 dB). The effectiveness of the online IS monitoring based on the internal impedance of the PV panel is verified as well.**

***Index Terms*—Compensation controller, Cooperative control, Online impedance spectroscopy,Power converter, PV panels.**

## I. Introduction

PHOTOVOLTAIC (PV) panels play a crucial role in nowadays' microgrid applications [1], [2]. The rising demand for reducing greenhouse gas emissions and growing adoption of renewable energy sources have led to a significant increase in the installation of PV panels. However, due to the environmental threats or human factors, PV panels may experience various faults during operation. These faults can make a detrimental impact on power generation, and even pose security risks, such as short circuits and fire hazards [3]. To mitigate these issues and improve the overall operating reliability of PV panels, health monitoring becomes just as essential as the energy management issues in microgrid applications [4]. Health monitoring tools for PV panels can be generally classified into two categories based on the type of characterization signals, i.e., visual and thermal tools, and electrical tools. Visual and thermal tools need the imaging devices, including lock-in thermography (LIT) [5], ultraviolet fluorescence (UVFL) imaging [6], photoluminescence (PL) imaging [7], electroluminescence (EL) imaging [8], [9], and infrared thermal (IR) imaging [10]. Meanwhile, the electrical tools involve analysing the electrical information obtained and most of them do not need additional equipment, such as I-V curves [11]–[13], spread spectrum time-domain reflectometry (SSTDR) [14], estimating randomness in the voltage signal (ERV), frequency spectrum analysis (FSA) [15] and impedance spectroscopy (IS) [16]. A comparison of these existing characterization tools is summarized in Table I, in terms of signal types, online/offline nature and cost, and typical applications.

It can be observed that visual and thermal tools require external equipment to capture visual or thermal information. Due to the high cost associated with the equipment, they are more suitable either for offline characterization of PV cells/panels under dark conditions on a laboratory scale or for online monitoring of large PV stations. For electrical tools, SSTDR, ERV and FSA are online tools but are limited to arc fault detection in PV arrays. Workstation-based IS can be applied offline or online, but it is preferred for offline applications due to the high cost and considerable volume of the specific workstation. Moreover, it is generally designed for the characterizations of PV materials, single PV cells, or small-size PV panels with relatively low compatible voltage and current levels. Both I-V curves and converter-based IS can provide rich health information about PV panels, while no additional equipment is required. However, I-V curves require the current and voltage information over the entire voltage range (between open circuit and short circuit), and the PV panels' output power is much affected during the monitoring period. On the other hand, converter-based IS is applied at a steady-state operating point which can maintain quasi-maximum output power even during its implementation, which is a desirable feature for microgrid applications. It

This work was supported by French national agency (ANR) project JCJC EREMITE (Grant number: ANR-19-CE05-0008-01) and Chinese Scholarship Council (Corresponding author: Zhixue Zheng).

X. Wang, Z. Zheng, M. Aillerie, J.P. Sawicki, and A. De Bernardinis are with Université de Lorraine, CentraleSupélec, Laboratoire Matériaux, Optique, Photonique et Systèmes, LMOPS, F-57070 Metz, France (e-mail: xin.wang@univ-lorraine.fr; zhixue.zheng@univ-lorraine.fr; michel.aillerie@univ-lorraine.fr; jean-paul.sawicki@univ-lorraine.fr; alexandre.de-bernardinis@univ-lorraine.fr). M.C. Péra and D. Hissel are with Université de Franche-Comté, FEMTO-ST, FCLAB, CNRS, Belfort, France (e-mail: marie-cecile.pera@univ-fcomte.fr; daniel.hissel@univ-fcomte.fr).

TABLE I
COMPARISON OF EXISTING CHARACTERIZATION TOOLS FOR PV APPLICATIONS

| Categories | Typical tools | Signal types | Online/offline and cost | Applications |
|---|---|---|---|---|
| Visual and thermal tools | LIT [5] | Infrared image | Offline (open circuit/dark condition) Infrared-sensitive camera | PV cell |
| | UVFL imaging [6], PL imaging [7] | UVFL image, PL image | Offline (open circuit/dark condition) UV light source/laser source, camera | PV cell |
| | EL imaging [8], [9] | EL image | Offline (open circuit) Infrared-sensitive camera | **PV panel** |
| | IR imaging [10] | Infrared image | **Online** Thermal camera | Large PV station |
| Electrical tools | I-V curves [11]–[13] | Voltage, current | Offline (open to short circuit) No additional equipment | **PV panel** |
| | SSTDR [14] | Voltage, current | **Online** Additional power generator | PV array |
| | ERV, FSA [15] | Voltage, current | **Online** No additional equipment | PV array |
| | Workstation-based IS [24] | Voltage, current | Offline/online Specific workstation | PV cell, small-size PV panel |
| | Converter-based IS [16] | Voltage, current | **Online** No additional equipment | **PV panel** |

has been proven effective in health monitoring of energy systems such as fuel cells and batteries [16]–[22], but it is rarely applied in PV panels. More specifically, most faults in PV panels occur within a short time scale, which requires a broader frequency range of the perturbation signal, and the maximum frequency of the perturbation signal should be at least 1 kHz [23]. The control strategy of the power converter should be specifically designed to ensure a stable broadband perturbation signal injection.

Generally, the control of the perturbation signal can be achieved in two ways: open-loop control and closed-loop control. Open-loop control applied a small perturbation signal directly to the duty cycle and offers the advantages such as control simplicity and tracking rapidity [16], [19], [20], [25]. However, due to the nonlinear relationship between the small-signal duty cycle and the resulted perturbation current of the PV panel, the amplitude of the perturbation current cannot be kept constant. This amplitude variation can impact the accuracy and even the validity of the IS measurements. Indeed, intrinsic resonance may occur in power converters especially under broadband perturbations [26]. On the other hand, closed-loop control applies a compensation controller to maintain a constant amplitude for the perturbation signal, ensuring reliable and accurate IS measurements. Nevertheless, the compensation controller should be specifically designed to meet requirements such as tracking accuracy, control bandwidth, and control stability.

In the literature, closed-loop control methods for converters can be generally categorized into three categories: single-loop voltage control, single-loop current control and voltage-current dual-loop control. Single-loop voltage control directly regulates the perturbation voltage, and it may suffer from stability issues [27]. Meanwhile, dual-loop control typically combines an inner current loop with an outer voltage loop, and can greatly improve control stability. However, its control bandwidth is much limited due to the coupling design between the inner and outer loops. Typically, the crossover frequency of the outer loop should be at least five times smaller than that of inner loop. For IS implementation in PV panels, single-loop current control provides a higher bandwidth and better stability compared to the other two control methods, and thus is the focus hereafter.

Numerous closed-loop control methods have been presented in the literature for the IS implementation, depending on the specific requirements of the target systems. Authors in [18] analyzed amplitude distortions in open-loop control of a boost converter, and designed a compensated current control method using a proportional-integral (PI) controller to obtain the internal impedances of two lithium-ion batteries. The achieved frequency range for the perturbation signal is [0.1 Hz, 1 $k$Hz]. However, the PI controller herein was heuristically tuned. No design principle was outlined for the controller in order to meet a high tracking accuracy and a wide enough bandwidth for IS measurements. In [17], a closed-loop step-function perturbation of the output voltage of a bidirectional buck/boost converter is applied for online IS measurements of batteries. The perturbation frequencies of the step function used are from 10 Hz to 1 $k$Hz. In this study, the compensator controller type was not specified. Moreover, a high sampling rate of at least 100 times larger than the highest perturbation frequency was required to ensure accurate representations of the AC voltage and current waveforms. In [21], a controller design for fault diagnosis and load balancing of fuel cells based on IS measurements was introduced. The controller parameters were calculated based on the transfer function of a conventional boost converter, and the target frequency range was [0.1 Hz, 1 $k$Hz]. However, the design criteria and limitations were not clearly stated. A combination of a PI

controller with a resonant controller was proposed in [28], to achieve a higher frequency of the perturbation signal than the converter's crossover frequency for a fuel cell sysetm. This method controlled the DC and AC components separately, with a particular focus on the resonant controller's design. However, the division of the DC and AC components was not emphasized, and only four impedances at 100Hz, 500 Hz, 1 $k$Hz and 2 $k$Hz were measured. In [29], an adaptive amplitude-modulated pseudo-random binary sequence excitation method was proposed to improve the accuracy of IS measurements. However, the injection point was located at maximum output power point (MPP), which seemed to violate the linearity criterion required for IS measurement. This could impose certain limitations for PV panels exhibiting strong nonlinearity in proximity to the MPP.

In this work, to achieve a wide bandwidth for injecting the perturbation signal into the PV panel, single-loop current control method is mainly focused on. Meanwhile, to ensure a cooperative control between maximum power point tracking (MPPT) and IS modes, the DC component control of the PV panel current is jointly designed as well. The aim of this work is to provide a comprehensive design guideline for control strategies of converter-based IS, while ensuring a maximum/quasi-maximum output power throughout the entire operation. Based on the distinct characteristics of three compensation controllers, i.e., proportional (P), PI and quasi-proportional resonant (QPR) controllers, two control strategies were designed and compared both in theory and experiment. The major contributions can be summarized as follows:

- Proposal of a cooperative control scheme of MPPT and IS modes. Compared with the commonly used I-V curves for PV panels, which requires an entire voltage sweep between open-circuit and short-circuit, IS is implemented at a steady-state operating point. Quasi-maximum PV panel output power can be guaranteed even during IS monitoring mode.
- Systematic design and comparison of two control strategies, i.e., unified control and separated control, for both the DC component and AC perturbation signal control. In the separated control strategy, a segmented low pass filter (LPF) with a variable cut-off frequency, which separates the DC and AC components, is proposed to ensure both the tracking accuracy and control speed of the control loops.
- Online experimental verification and comparison of the designed control strategies. In the experimental tests, a set of IS measurements are acquired online with high tracking accuracy and sufficient signal-to-noise ratio (SNR) in the frequency range of [1 Hz, 2 $k$Hz]. Meanwhile, as an illustration, the operating states such as different irridiance levels, can be reflected effectively by the evolution of internal impedance.

The remaining sections of this article are organized as follows: Section II briefly explains the cooperative control scheme between MPPT and IS modes. The IS measurement principles together with its validity criteria are introduced for PV panel online characterization. Meanwhile, the characteristics of a conventional boost converter is described based on its transfer function. In Section III, two control strategies based on three compensation controllers are designed and compared. The control parameter design of the three controllers together with that of the LPF are introduced in detail. Online experimental implementation, verification and comparison of both control strategies are presented in Section IV. Finally, conclusions and discussions are drawn up in Section V.

## II. System Description

### A. Cooperative control scheme of MPPT and IS modes

Fig. 1 illustrates a simplified microgrid topology. A PV panel supplies power to the load through a step-up DC/DC converter, e.g., a boost converter. The energy storage system is connected to the DC bus by a bi-directional DC/DC converter. And the DC bus voltage is maintained stable under different operating conditions by controlling the charging and discharging of the storage system. By regulating the switching signals of the DC/DC converter connected with the PV panel, the operating point of the PV panel can be adjusted, according to its operating modes, either in MPPT mode or IS mode. IS measurement requires that a perturbation signal is injected around a steady-state operating point. The stabilization of the system before and after the perturbation is necessary for the validity of IS measurement. Therefore, an intermediate mode, which is named injection point tracking (IPT) mode, is added between MPPT and IS modes to confirm that the PV panel operates stably at the injection point before the perturbation signal injection. The proposed cooperative control scheme is shown in the converter control block in Fig. 1, and a simplified overall control flow chart of the control scheme is illustrated in Fig. 2.

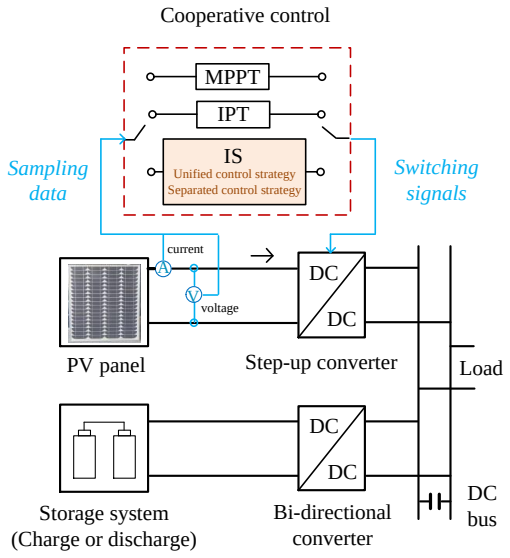


Fig. 1. Overall cooperative control scheme between MPPT and IS modes

Normally, the PV panel is controlled in MPPT mode based on the control principle of the cooperative control scheme. A variable-step perturb and observe (P&O) method is utilized herein to realize the MPPT mode [30]. When the system

starts health monitoring (e.g., a trigger signal is activated), the control scheme switches firstly to the IPT mode to run the PV panel from the MPP to the injection point. A classical PI controller is applied in IPT mode which follows the same designing principle of DC component control in Section III.C. Once the voltage and current of the PV panel are stabilized, a perturbation signal is injected, and the IS mode is initiated. In IS mode, the PV panel is controlled at a steady-state injection point (thus, it can be considered as a linear system) with a small perturbation signal by either the unified or the separated control strategy (more details are provided in Section III), to ensure simultaneously the continuity of output power and online IS measurement. After completing the required number of repetitions of IS measurements, the PV panel returns to the MPPT mode until the next health monitoring cycle.

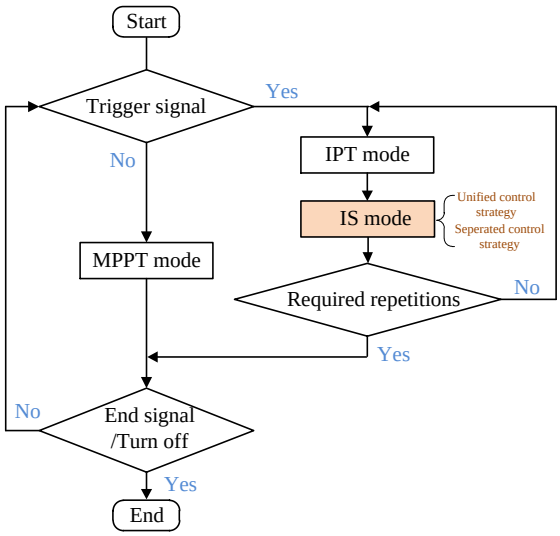


Fig. 2. Simplified overall control flow chart of the cooperative control scheme

### B. IS measurement principles

IS characterizes the system dynamic property in the frequency domain by superimposing a small perturbation signal with a variable frequency on a steady-state operating point. As indicated in Fig. 3 (a), according to the changing rate of $I_{pv}$ with $V_{pv}$, a typical I-V curve of silicon PV panel can be divided into three operating regions: a quasi-linear current source region (I), one nonlinear power region (II), and a quasi-linear voltage source region (III). A perturbation current (or voltage) signal is injected into a steady-state operating point located in the system linear/quasi-linear operating region (i.e., region I or III), and the response voltage (or current) is collected. Based on the measured current and response voltage signal, the PV panel's internal impedance $Z_{PV}(f_p)$ can be calculated as:

$$Z_{PV}(f_p) = \frac{V_{ac}(f_p)}{I_{ac}(f_p)} e^{j\Theta_z(f_p)} \tag{1}$$

where $f_p$ is the frequency of the perturbation signal, $V_{ac}(f_p)$ and $I_{ac}(f_p)$ are the amplitudes of the AC components of PV panel voltage and current at frequency $f_p$, respectively; $\Theta_z(f_p)$ represents the phase of PV panel's internal impedance at frequency $f_p$, which is the phase shift between the voltage and current signals:

$$\Theta_z(f_p) = \Theta_v(f_p) - \Theta_i(f_p) \tag{2}$$

where $\Theta_v(f_p)$ and $\Theta_i(f_p)$ represent the phases of the voltage and current signals, respectively.

To ensure the validity of IS measurements, four mathematical criteria, including linearity, causality, stability and finiteness, must be met [31]. Generally, these criteria can be verified by passing a Kramers-Kronig (K-K) test. Herein, the significance of linearity and stability in the online implementation of IS for PV panels is specially emphasized.

- **Linearity**. To guarantee the linearity, the PV panel should operate in a linear/quasi-linear region as indicated by points A and B in Fig. 3 (a). Meanwhile, two cautions should be noted. Firstly, the amplitude of the perturbation signal should not be too large to disturb the PV panel from equilibrium. Secondly, the amplitude should be larger than the system inherent noises to guarantee a good SNR. A suggested range for the amplitude of the perturbation signal is 5% - 15% of the DC component [32].
- **Stability**. The stability condition requires that the system works in the same stable state before and after the perturbation. To respect this condition, the operating conditions (e.g., the irradiance levels and temperatures) of the PV panel should be kept unchanged during the IS implementation. Meanwhile, the PV panel should be brought to a steady-state operating state before starting each impedance measurement. It must also return to the original state once the perturbation has disappeared. That also explains why an IPT mode is added between MPPT and IS modes. This criterion can be verified by repeating the measurements and checking their consistency. Hence, in our experimental verification, at least five IS measurements are repeated under the same operating condition.

As for the choice of the injection region, the major considerations are as follows. In region I, taking A as injection point, it can be observed that since the variation range of the PV current is relatively narrow, it is difficult to obtain an AC current of sufficient amplitude whether as a perturbation signal or a response signal. On the other hand, taking B in region III as an injection point, it can be observed that due to the relatively large variation range of the voltage and current, it would be more flexible to inject the perturbation signal in either the form of current or voltage. Therefore, the region III is selected as the injection region. As analyzed in the introduction, closed-loop current control method is the major focus of this work, AC current is thus selected as the perturbation signal.

According to (1), the IS measurement of the PV panel can be calculated and plotted, as illustrated in Fig. 3 (b). Combined with an equivalent circuit model (ECM), the corresponding internal parameters can be extracted, which can describe the health states of the PV panel. A typical ECM of the PV panel is shown in Fig. 3 (c). It corresponds to a Nyquist plot with a single time constant (with the corresponding frequency $f_0 =$

$1/(2\pi R_p C_p)$) of a resistance $R_p$ in parallel with a capacitor $C_p$, which is shifted from the origin by a series resistance $R_s$, as indicated in Fig. 3 (b) [1], [16]. Theoretically, once the impedance at $f_0$ is obtained, the value of $R_s$ can be determined by curve fitting methods even without a complete spectrum [33], as indicated by the dashed line.

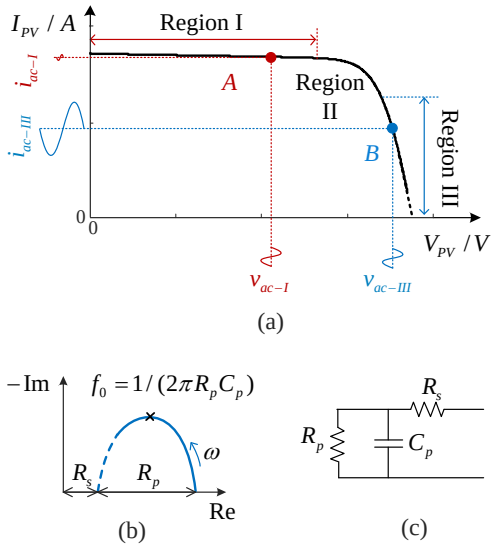


Fig. 3. IS measurement principle and AC equivalent circuit

### C. Characteristics of a conventional boost converter

Conventional boost converter is a commonly used step-up converter in microgrids, with its topology shown in Fig. 4. By ignoring the circuit parasitic parameters, the corresponding symbols and parameters are listed as follows: $S$-the input voltage source, $v_{in}$ and $i_L$ - the input voltage and inductor current of converter, $L$ - the inductor, $T$ and $d$ - the switch and its duty cycle, Diode - the diode, $C$ - the DC bus capacitor, $V_o$ and $R_L$ - the DC bus voltage and the load.

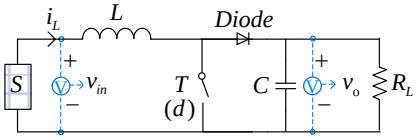


Fig. 4. Conventional boost converter with turned-off switch

The system's state-space average model can be expressed as:

when $T$ is turned on:

$$\begin{cases} \dot{x} = A_1 x + B_1 v_{in} \\ v_o = C_1 x \end{cases} \tag{3}$$

when $T$ is turned off:

$$\begin{cases} \dot{x} = A_2 x + B_2 v_{in} \\ v_o = C_2 x \end{cases} \tag{4}$$

where $x = [i_L v_o]^T$, and the $\dot{x}$ means its time derivative. The parameters' arrays are specified as:

$$A_1 = \begin{bmatrix} 0 & 0 \\ 0 & -\frac{1}{C \cdot R_L} \end{bmatrix}, B_1 = \begin{bmatrix} \frac{1}{L} \\ 0 \end{bmatrix},$$

$$A_2 = \begin{bmatrix} 0 & -\frac{1}{L} \\ \frac{1}{C} & -\frac{1}{C \cdot R_L} \end{bmatrix}, B_2 = \begin{bmatrix} \frac{1}{L} \\ 0 \end{bmatrix},$$

$$C_1 = \begin{bmatrix} 0 & 1 \end{bmatrix}, C_2 = \begin{bmatrix} 0 & 1 \end{bmatrix}.$$

When the boost converter operates in continuous-current mode (CCM), its overall state-space average model by summing both states can be written as:

$$\begin{cases} \dot{x} = [A_1 d + A_2(1-d)]x + [B_1 d + B_2(1-d)]v_{in} \\ v_o = [C_1 d + C_2(1-d)]x \end{cases} \tag{5}$$

Considering a direct small-signal perturbation on duty cycle, the following substitutions can be made, i.e., $d = D + \hat{d}$, $x = X + \hat{x}$, $v_{in} = V_{in} + \hat{v}_{in}$, $v_o = V_o + \hat{v}_o$. The state-space model in (5) can be linearized around a steady-state duty cycle $D$, state vector $X$, input voltage $V_{in}$, and DC bus voltage $V_o$. Therefore, the converter's response to the small-signal perturbation can be expressed as:

$$\begin{cases} \dot{\hat{x}} = [(A_1 - A_2)X + (B_1 - B_2)V_{in}]\hat{d} \\ \qquad + [A_1 D + A_2(1-D)]\hat{x} + [B_1 D + B_2(1-D)]\hat{v}_{in} \\ \hat{v}_o = [C_1 D + C_2(1-D)]\hat{x} + (C_1 - C_2)X\hat{d} \end{cases} \tag{6}$$

Where $\hat{d}$ is the small-signal perturbation on $D$, $\hat{x}$ and $\dot{\hat{x}}$ are the resulted perturbations on the state variable vector and its time derivative, $\hat{v}_{in}$ and $\hat{v}_o$ are the corresponding perturbations on the input voltage and DC bus voltage, and the differential products, i.e., $\hat{d}\hat{x}$, and $\hat{d}\hat{v}_{in}$, are ignored herein.

To study the influence of the duty cycle perturbation on the output current of the PV panel (i.e., $i_L$), the transfer function of small-signal duty cycle to the inductor current is calculated as:

$$\begin{aligned} G_{i_L - d}(s) &= \frac{\hat{i}_L}{\hat{d}}|_{\hat{v}_{in}=0} \\ &= K_{sys} \cdot \frac{s/\omega_{z-sys} + 1}{s^2/{\omega_{0-sys}}^2 + 2\zeta s/\omega_{0-sys} + 1} \end{aligned} \tag{7}$$

where $\omega_{z-sys} = 2/R_L C$ and represents the frequency of the zero of the transfer function $G_{i_L-d}(s)$; the gain of the system $K_{sys}$, the system natural frequency $\omega_{0-sys}$ and damping ratio $\zeta$ satisfy the following conditions:

$$\begin{aligned} K_{sys} &= 2V_{in}/((1-D)^3 R_L), \\ \omega_{0-sys} &= (1-D)/\sqrt{LC}, \\ \zeta &= 1/(2R_L C \omega_{0-sys}) \end{aligned}$$

Based on (7), the open-loop gain of the conventional boost converter is drawn in MATLAB, as shown in Fig. 5. As an example, the system parameters are set as: $D$ = 0.5, $C$ = 260 $uF$, $L$ = 2.5 $mH$, $V_{in}$ = 33 $V$, $R_L$ = 96 Ω (more details on the experimental setup are further given in Section III). Fig. 5 exhibits a nonlinear relationship between the amplitude of the perturbation current and the perturbation duty cycle, i.e. $G_{i_L-d}$ as the frequency changes. A peak caused by the series

connection of the inductor $L$ and the DC bus capacitor $C$ when the switch is off appears at the resonant frequency $f_{res}$ [26]:

$$f_{res} \approx \frac{1-D}{2\pi\sqrt{LC}} = \frac{\omega_{0-sys}}{2\pi} \approx 98.7Hz \tag{8}$$

$f_c$ represents the crossover frequency of the system, and can be calculated by:

$$f_c \approx \frac{V_{in}}{2\pi(1-D)L} \approx 4.2kHz \tag{9}$$

Due to the peak at $f_{res}$ and the decrease in the magnitude of $G_{i_L-d}$ with increasing frequency, the linearity and accuracy of IS measurement will be affected. Therefore, it is necessary to add controllers to compensate for system control.

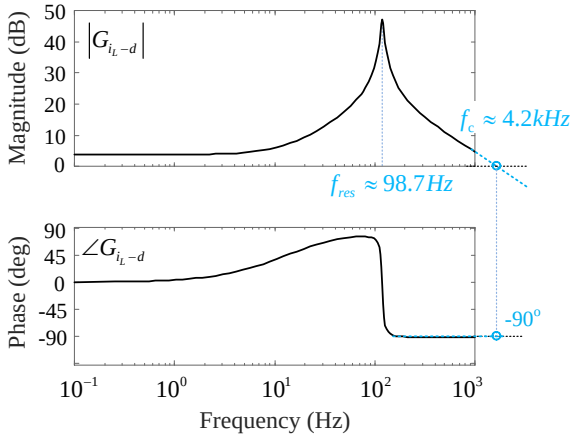


Fig. 5. Bode plots of the open-loop transfer function $G_{i_L-d}$

## III. Control Strategies for Converter-Based IS Implementation

As introduced in Section II, due to the intrinsic resonance of the boost converter under broadband perturbations, a suitable compensation controller is necessary to guarantee a stable perturbation signal with a constant amplitude. This section focuses on the design of closed-loop current control based on three commonly used compensation controllers in linear system control, i.e., P, PI and QPR controllers. The main consideration is that, during IS implementation, the PV panel operates at a steady-state operating point located within the linear/quasi-linear operating region.

### A. Control objectives

The closed-loop current control block diagram without compensation is shown in Fig. 6, where the blue lines represent the sampling current and the duty cycle, corresponding to the sampling data and the switching signals in Fig. 1. Its corresponding uncompensated closed-loop gain is depicted in Fig. 7. As can be observed in the figure, a static error exists at very low frequencies. Using the same system parameters in Section II, the corresponding static error reaches 36.2%. When the frequency of the perturbation signal is higher than the crossover frequency, i.e., $f_c$, the amplitude of the actual current signal is significantly lower than the reference value. It means that in an uncompensated control system, there is a deviation in the location of the injection point. The value of $f_c$ can limit the bandwidth of the perturbation current signal. Therefore, to achieve reliable broadband IS measurements in PV panels, a compensation controller is necessary and should meet the following requirements:

- High open-loop gain at 0 Hz. It should be as high as possible to ensure a stable operating condition of the PV panel during IS implementation;
- Large crossover frequency. It should be sufficiently extended to ensure a wide bandwidth for the perturbation current signal;
- High tracking accuracy. The reference of the perturbation signal should be tracked with high accuracy to prevent the operating points from entering the nonlinear region during IS implementation;
- Stable control system. It is necessary to ensure that the system meets the stability criteria during IS implementation – the control system has sufficient phase margin ($> 30^o$) and gain margin ($> 6$ dB), or all the poles of the closed-loop transfer function lie in the left-half plane.

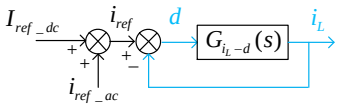


Fig. 6. Closed-loop current control without compensation

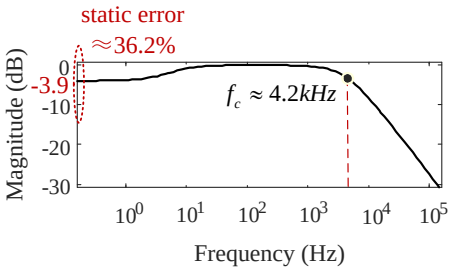


Fig. 7. Magnitude plot of the closed-loop transfer function without compensation

In order to meet the control objectives, it is essential to choose an appropriate controller for compensation. P, PI and proportional resonant (PR) controllers are three commonly used compensation controllers in linear system control [34]. Due to the presence of sampling errors, the PR controller is often replaced by the QPR controller in practical uses [35]. Hence, the QPR controller instead of the PR controller is analyzed in this study. The transfer functions of the three controllers can be expressed separately as follows:

P controller:

$$G_P(s) = K_p \tag{10}$$

PI controller:

$$G_{PI}(s) = K_{pi}(1 + \frac{\omega_{z-pi}}{s}) \tag{11}$$

QPR controller:

$$G_{QPR}(s) = K_{qpr} + \frac{K_r \omega_{c-qpr} s/\omega_{res-qpr}^2}{\frac{s^2}{\omega_{res-qpr}^2} + \frac{2s\omega_{c-qpr}}{\omega_{res-qpr}^2} + 1} \tag{12}$$

where $K_p$, $K_{pi}$ and $K_{qpr}$ represent the proportional factor of the P, PI and QPR controller, respectively; $\omega_{z-pi}$ is the angular frequency when the phase angle of PI controller is equal to $-45^o$; $\omega_{res-qpr}$ represents the angular resonant frequency of the QPR controller, $\omega_{c-qpr}$ and $K_r$ denote the gain bandwidth and peak gain at the resonance point, respectively.

Based on the transfer functions, the asymptotic magnitude and phase plots of the three controllers are depicted in Fig. 8. The P controller has only a proportional factor and can be sufficient to achieve the desired crossover frequency with an adequate phase margin. However, the gain remains constant across the entire frequency range.

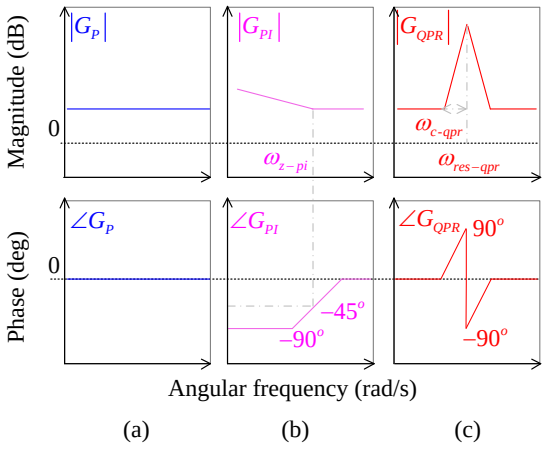


Fig. 8. Asymptotic Bode plots of P, PI and QPR controllers (upper: magnitude plots; lower: phase plots)

Due to the pole at the origin and the zero at $f_{z-pi} = \omega_{z-pi}/2\pi$, the gain of the PI controller can theoretically reach an infinite value and the phase is smaller than $0^o$, when the frequency is going down to 0 Hz. The QPR controller, on the other hand, adds one resonant part. Its two conjugate poles result in a significant gain at $f_{res-qpr} = \omega_{res-qpr}/2\pi$. The gain at other frequencies depends on the value of $K_{qpr}$. A suitable bandwidth of the QPR controller can be achieved by adjusting accordingly the value of $\omega_{c-qpr}$.

In summary, the PI controller can track DC signals without static errors, but the phase margin of the system may be influenced. The P controller has the simplest structure, but exhibits an error in the location of the injection point, which affects the accuracy of IS measurement. The QPR controller can only track signals with a frequency of $f_{res-qpr}$ with high accuracy. To achieve the control objectives of converter-based IS, closed-loop control strategies relying on the three compensation controllers can be categorized into two classes:

1) Unified control strategy, which utilizes a single controller to achieve all the aforementioned requirements. In this strategy, the DC component, i.e., the injection point, and the AC component, i.e., the perturbation signal, are controlled in a unified way;
2) Separated control strategy, which utilizes a combination of controllers in cases where a single controller cannot satisfy all the requirements. In this strategy, the DC and AC components are controlled separately.

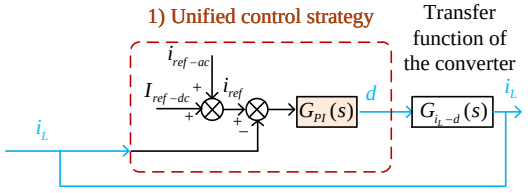


(a) Unified control strategy with a single PI controller

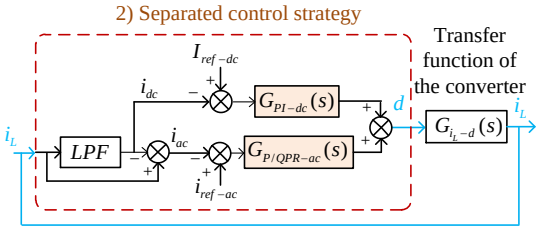


(b) Separated control strategy with a PI controller and a P/QPR controller

Fig. 9. Two control strategies based on the PI and P/QPR controllers

According to the characteristics analyzed above, the overview of the two control strategies' control blocks is illustrated in Fig. 9, where the dashed red box indicates the control blocks; $i_{ref}$, $i_{ref-dc}$ and $i_{ref-ac}$ represent the total current reference, DC component reference and AC component reference, respectively; the shading block represent the different controllers; LPF means the low-pass filter. More details on the design of the two control strategies and the setting of the corresponding control parameters are given in the following parts.

### B. Unified control strategy

As indicated in Fig. 8, the PI controller exhibits an infinite gain when the frequency is going down to 0 Hz and the system's crossover frequency can be sufficiently extended by adjusting the controller's parameters. It is possible to meet all the aforementioned requirements for IS implementation based on a single PI controller. Therefore, it is chosen for the unified control strategy, as shown in Fig. 9 (a).

The open-loop transfer function of the system with a single PI compensation controller can be described as:

$$H_{PI}(s) = G_{PI}(s) \cdot G_{i_L-d}(s) \tag{13}$$

At high frequencies (i.e., $\omega \gg \omega_{0-sys}$), by substituting (7), the compensated gain can be approximated as:

$$\begin{aligned} |H_{PI}(s)| &= |G_{PI}(s)| \cdot |G_{i_L-d-h}(s)| \\ &\approx |G_{PI}| \cdot K_{sys} \cdot \frac{\omega_{0-sys}^2}{\omega_{z-sys} \cdot \omega_{inj}} \end{aligned} \tag{14}$$

where $|G_{i_L-d-h}(s)|$ represents the gain of $G_{i_L-d}(s)$ at high frequency; $\omega_{inj}$ is the angular frequency of the perturbation signal. The maximum value of $\omega_{inj}$, denoted as $\omega_{inj-max}$, is determined by both the system parameters and the steady-state operating point. For example, based on the parameters used in Section II.C, the maximum variation value of the small-signal duty cycle can reach 0.5 without over-modulation. Assuming that the DC component at the injection point is equal to 1 $A$, to obtain a perturbation current signal with an amplitude of 0.15 (15% of the DC component), $\omega_{inj-max}$ can reach $8.8 \times 10^4$ rad/s (i.e., around 14 $k$Hz) based on (7). This limited value caused by the system parameters and steady-state operation can be denoted as $\omega_{inj-max-sys}$. In actual operation, $\omega_{inj-max}$ will be smaller than the ideal situation, due to the influence of parasitic parameters [26].

The relationship between the inductor current (i.e., $i_L$) and the reference current (i.e., $i_{ref}$) shown in Fig. 9 (a) is:

$$i_L = i_{ref} \cdot \frac{|H_{PI}(s)|}{1 + |H_{PI}(s)|} \tag{15}$$

Based on (15), to ensure that the current control loop is effectively compensated, the compensated gain, denoted as $|H_{PI}(s)|$, must meet: $|H_{PI}(s)| \geq 9$. This condition guarantees $i_L/i_{ref} \geq 90\%$, thus keeping the tracking error of perturbation signal smaller than $10\%$, and (14) can be further expressed as:

$$|G_{PI}(s)|_{\omega_{inj-max}} \cdot K_{sys} \cdot \frac{\omega_{0-sys}^2}{\omega_{z-sys} \cdot \omega_{inj-max}} \geq 9 \tag{16}$$

To ensure a sufficient control bandwidth, the target crossover frequency, denoted as $\omega_{ct}$, should be greater than the the value of $\omega_{inj-max}$. According to the definition of the crossover frequency (i.e., the frequency at which the open-loop gain reaches the value 1) and (14), the gain of the compensated current control loop at $f_{ct}$ should satisfy:

$$|G_{PI}(s)|_{\omega_{ct}} \cdot K_{sys} \cdot \frac{\omega_{0-sys}^2}{\omega_{z-sys} \cdot \omega_{ct}} = 1 \tag{17}$$

Therefore, $\omega_{inj-max}$ should be $\leq (1/9) \cdot \omega_{ct}$ based on (16) and (17), while subject to the system constraints. Meanwhile, to mitigate the switching noise, the target crossover frequency, i.e., $\omega_{ct}$, should be theoretically less than half of the switching frequency in angular form, denoted as $\omega_{sw}$. The relationship between $\omega_{inj-max}$, $\omega_{ct}$ and $\omega_{sw}$ can thus be expressed as:

$$\omega_{inj-max} \leq min[\frac{1}{9}\omega_{ct}, \quad \omega_{inj-max-sys}] < \frac{1}{2}\omega_{sw} \tag{18}$$

where $\omega_{sw} = 2\pi \cdot f_{sw}$.

The switching frequency $f_{sw}$ is set as 80 $k$Hz in the experimental setup due to the hardware limitations. According to (18), $\omega_{ct}$ is set as between [1/4, 1/5] of $\omega_{sw}$, e.g., $2\pi \times 1.8 \times 10^4$ rad/s, to reduce sufficiently switching noise in actual operation. $\omega_{inj-max}$ is the thus set as $2\pi \times 2 \times 10^3$ rad/s. The frequency range of the perturbation current signal is thus set within the range of [1 Hz, 2 $k$Hz]. By setting the target crossover frequency in the *pidtune* function in MATLAB, $K_{pi}$ and $\omega_{z-pi}$ can be calculated as: $K_{pi} = 4.28$, $\omega_{z-pi} = 1.98 \times 10^3$, with a sufficient phase margin (i.e., $90^o$) to guarantee the system's stability. It should be noted that the parameters satisfying the requirements of stability and control targets are not just one set, but a range. Moreover, during practical applications, the controller parameters may need further tuning due to the influence of system parasitic parameters, potential noises and uncertainties. However, the theoretical values calculated herein can still serve as reference values. The same comment applies to the following controller parameters.

### C. Separated control strategy

As analyzed in Section III.A, the P controller amplifies the entire frequency range signal with the same proportional factor but cannot eliminate the static errors when the frequency decreases to 0 Hz. Meanwhile, the QPR controller can only achieve accurate control at its resonant frequency. Therefore, both controllers require an additional section to control the DC component to ensure the stability of the injection point. When applying the two controllers, a combined control is thus necessary, and two control loops for the DC and AC components control should be designed separately, which is thus named as separated control strategy.

In this strategy, as indicated in Fig. 9 (b), a PI controller with a narrow control bandwidth can realize the DC component (i.e., $i_{dc}$) tracking without static errors, while P or QPR controllers is used to control the AC component (i.e., $i_{ac}$). It should be noted that, to separate effectively the original current signal (i.e., $i_L$) into DC and AC components, a first-order LPF is added in the current feedback path and its parameters should be carefully designed to ensure both the tracking accuracy and the control speed of the control loops.

*1) LPF design:* The transfer function of the LPF can be written as:

$$G_{LPF}(s) = \frac{1}{1 + s/\omega_{0-LPF}} \tag{19}$$

where $\omega_{0-LPF}$ is the cut-off frequency. The attenuation of the signal (i.e., $i_L$) at $\omega_{0-LPF}$ is -3 dB (approximately 70% times gain). The design principle of the LPF is to attenuate the AC component above $\omega_{0-LPF}$ as much as possible (with a sufficiently low $\omega_{0-LPF}$), while ensuring the control speed (with a sufficiently high $\omega_{0-LPF}$, as the settling time under unit step response is inversely proportional to $\omega_{0-LPF}$). Under broadband frequency perturbations, maintaining a constant $\omega_{0-LPF}$ can hardly achieve both significant attenuation of the AC component and sufficient control bandwidth.

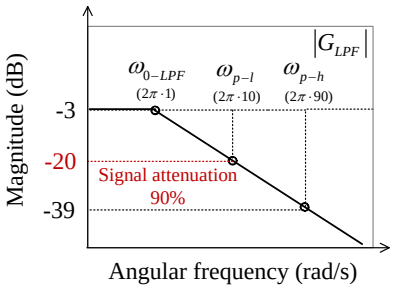


Fig. 10. Asymptotic magnitude plot of the LPF (example of $\omega_{p-l} = 2\pi \cdot 10$ rad/s, $\omega_{p-h} = 2\pi \cdot 90$ rad/s)

For simplicity of online control, perturbation frequencies are divided into several ranges. Consequently, a segmented LPF with a variable cut-off frequency is designed according to the defined range. Each frequency range can be expressed as $[\omega_{p-l}, \omega_{p-h}]$, where $\omega_{p-l} = 2\pi \cdot 10^{(i-1)}$, $\omega_{p-h} = 2\pi \cdot 10^{i} - 2\pi \cdot 10^{(i-1)}$, with an angular frequency interval of $2\pi \cdot 10^{(i-1)}$ and $i = 1, 2, 3, \cdots$. In each range, the $\omega_{0-LPF}$ of the LPF is set as 10% of the lower frequency limit (i.e., $\omega_{p-l}$) of the perturbation signal, corresponding to a gain of -20 dB (i.e., 10% times gain or 90% signal attenuation) as indicated in Fig. 10:

$$\omega_{0-LPF} = 0.1\omega_{p-l} \tag{20}$$

In this asymptotic magnitude plot of the LPF, the relationship between $\omega_{0-LPF}$, $\omega_{p-l}$ and $\omega_{p-h}$ is indicated. When (20) is satisfied, the perturbation signal within the range $[\omega_{p-l}, \omega_{p-h}]$ will be significantly attenuated by at least 90%.

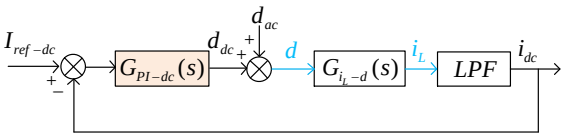


Fig. 11. Separated control strategy – DC component control based on a PI controller

*2) PI controller design for DC component control:* To set appropriate PI controller parameters, the input of AC component is considered as a disturbance and the corresponding control block diagram in Fig. 9 (b) can be simplified as Fig. 11. In this case, the transfer function of DC component open-loop current control can be written as:

$$\begin{aligned} H_{PI-dc}(s) &= G_{PI-dc}(s) \cdot G_{i_L-d}(s) \cdot G_{LPF}(s) \\ &= K_{pi-dc} \cdot \frac{(1 + \frac{\omega_{z-pi-dc}}{s})}{1 + \frac{s}{\omega_{0-LPF}}} \cdot G_{i_L-d}(s) \end{aligned} \tag{21}$$

where $G_{PI-dc}(s)$ represents the transfer function of the PI controller for DC component control. To further reduce the impact of residual perturbation signals on DC component control, the crossover frequency (i.e., $\omega_{c-dc}$) of DC component control system should be smaller than the perturbation frequency. Meanwhile, to ensure the tracking accuracy of the DC component, the attenuation of the perturbation signal must be sufficient. It means $\omega_{c-dc}$ should be greater than the cutoff frequency of the LPF (i.e., $\omega_{0-LPF}$), as indicated in Fig. 12.

Considering the selection of $\omega_{0-LPF}$ in the last subsection, $\omega_{c-dc}$ is expressed as:

$$\omega_{c-dc} = n \cdot \omega_{0-LPF} \tag{22}$$

where $n$ represents the proportional relationship between $\omega_{c-dc}$ and $\omega_{0-LPF}$, and belongs to [1, 9]. The maximum value of $n$ implies a fast control speed for the system, but stabilization may be challenging. In our study, the value of $n$ is selected as 5 during online experimental tests.

Based on (22), a group of appropriate parameters of PI controller can be calculated by the *pidtune* function in MATLAB. For example, the PI controller parameters can be set as: $K_{pi-dc}$ = 0.397, $\omega_{z-pi-dc}$ = 60.45 to achieve the crossover frequency of 5 Hz, which can effectively filter out the residual perturbation signal within the range [10 Hz, 90 Hz] and also ensure the DC component tracking accuracy. With the set parameters, all the poles of the closed-loop transfer function shown in Fig. 11 lie in the half-left plane which ensures the system stability.

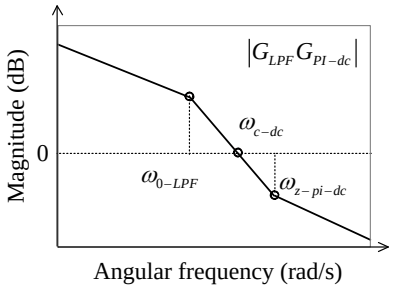


Fig. 12. Asymptotic magnitude plot of DC component control with a PI controller

*3) P and QPR controller design for AC component control:* For the perturbation current signal control, the target is to achieve an open-loop gain as large as possible at the perturbation frequency. The DC component input is seen as a disturbance and the control block diagram can be simplified as Fig. 13. The transfer function of AC component open-loop control can be expressed as:

$$G_{ac}(s) = G_{P/QPR}(s) \cdot G_{i_L-d}(s) \cdot (1 - G_{LPF}(s)) \tag{23}$$

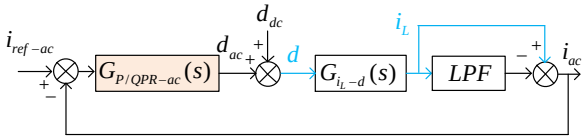


Fig. 13. Separated control strategy – AC component control based on a P/QPR controller

As introduced, the P controller amplifies the entire frequency range signal with the same proportional factor with an adequate phase margin. If a P controller is selected, for (23), the crossover frequency of the control system only needs to be less than half of the switching frequency. To ensure that the current control loop is effectively compensated, the compensated gain, denoted as $|H_P(s)|$, must meet: $|H_P(s)| \geq 9$, following the same principle as that of the unified control strategy. This condition guarantees $i_{ac}/i_{ref-ac} \geq 90\%$, thus keeping the tracking error smaller than 10%, even at $\omega_{inj-max}$, and can be further expressed as:

$$|H_P(s)|_{\omega_{inj-max}} = |\frac{s}{s + \omega_{0-LPF}} \cdot K_p \cdot G_{i_L-d}(s)|_{\omega_{inj-max}} \geq 9 \tag{24}$$

Under the same considerations as the unified control strategy, the target crossover frequency of the system should satisfy (18), if the P controller is selected in the separated control strategy. By applying the *pidtune* function in MATLAB, $K_p$ is set as 4.28 for the entire frequency range, i.e., [1 Hz, 2

$k$Hz], with a sufficient phase margin (i.e., $90^o$) to ensure the system stability.

If a QPR controller is selected, (23) is equal to:

$$G_{ac}(s) = G_{Com-QPR}(s) \cdot G_{i_L-d}(s) \tag{25}$$

where $G_{Com-QPR}(s)$ represents the compensation part, can be expressed as:

$$G_{Com-QPR}(s) = \frac{s}{s+\omega_{0-LPF}} \cdot G_{QPR}(s) \tag{26}$$

Its asymptotic magnitude plot is depicted in Fig. 14. According to (12), the gain of the QPR controller at the perturbation frequency $\omega_{inj}$ which is equal to $\omega_{res-qpr}$, is calculated as:

$$|G_{QPR}(s)|_{\omega_{inj}} = K_{qpr} + K_r/2 \tag{27}$$

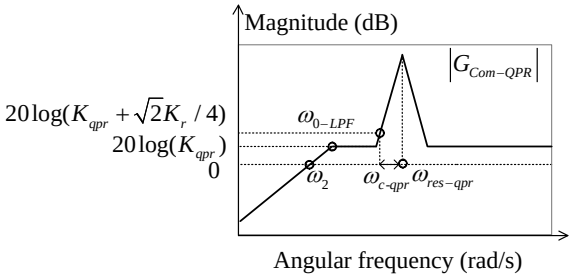


Fig. 14. Asymptotic magnitude plot of a QPR controller based compensation part of AC component control

In Fig. 14, $\omega_2$ affects the dynamic performance of the compensated system and its value is influenced by $K_{qpr}$. As $K_{qpr}$ increases, $\omega_2$ decreases, resulting in a better dynamic performance. Furthermore, the value of $K_{qpr}$ determines the amplification factor of signals beyond just the perturbation signals. It means that a lower value of $K_{qpr}$ will be beneficial to improve the SNR of the perturbation signals. $\omega_{c-qpr}$ represents the bandwidth of the QPR controller. A wider bandwidth can also increase the dynamic performance of the system, but will concurrently decrease the SNR of perturbation signals. However, in this application, IS implementation requires that the system operates at a steady-state operating point. The requirements for the dynamic performance are not very strict. Hence, a small $K_{qpr}$ is normally sufficient, and it is set as 0.2 herein. For $\omega_{c-qpr}$, a typical value is 5 rad/s. In practical applications, these two parameters can be appropriately increased according to the dynamic performance of the system. Based on the same designing criterion as in (24), the gain expressed in (25) should satisfy:

$$|H_{QPR}(s)|_{\omega_{inj}} = |G_{Com-QPR}(s) \cdot G_{i_L-d}(s)|_{\omega_{inj}} \geq 9 \tag{28}$$

Substituting (26) into (28) and the selected $K_{qpr}$, an appropriate range of $K_r$ can be obtained. For example, in our experiment, $K_{qpr} = 0.2$, the corresponding range of $K_r$ in the frequency range of [10 Hz ,90 Hz] is: $K_r \geq 2.87$.

Based on the above theoretical analysis, both control strategies, i.e., unified control and separated control, can realize the required control objectives for converter-based IS implementation. A summary and comparison of the characteristics of the three controllers, in terms of number of control parameters, control bandwidth and controller type, are given in Table II. The separated control strategy based on the QPR controller enables the widest control bandwidth for the perturbation signal while with the most control parameters, i.e., seven. The unified control strategy utilizing a single PI controller can achieve the same control bandwidth as the separated control strategy based on the P controller, while has a simpler design with only two control parameters. An experimental study is further conducted in the next section for online verification and comparison. The frequency range of the perturbation signal is uniformly set to [1 Hz, 2 $k$Hz] for both control strategies for fair comparison.

## IV. Experimental Verification

An experimental platform has been developed in the laboratory for converter-based online IS implementation, as shown in Fig. 15. The platform includes a PV panel (RECOM-SILLIA 60MXXX), a boost converter based on a half-bridge SiC power module (PEB 8024) with an integrated DC bus capacitor ($C$ = 260 $u$F) and in series with an inductor ($L$ = 2.5 $m$H), and a resistive output load ($R_L$ = 96 Ω). The current signal is collected by a high-precision current transducer (IT 65-S ULTRASTAB). The detailed information is listed in Table III. The perturbation signal and corresponding responses are generated and collected by a real-time control system (dSPACE SCALEXIO box).

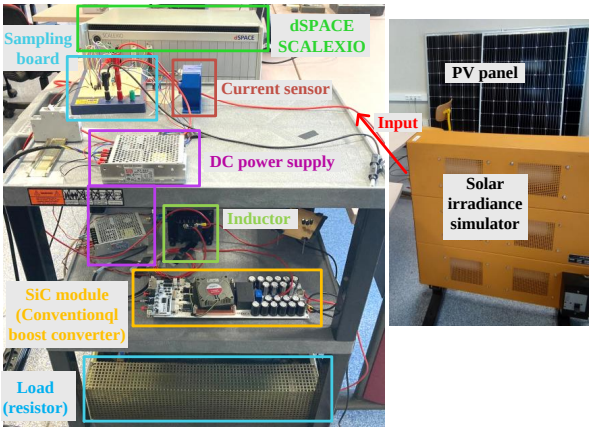


Fig. 15. Experimental platform for converter-based online IS implementation

For the IS implementation, the amplitude of the perturbation signal is set to 15 % of the DC component of the PV current to ensure the linearity criterion while favoring a higher perturbation frequency (i.e., $\omega_{inj-max}$) as discussed in Section II.B. The number of frequency points per decade is 10 for the frequency range [1 Hz, 1 $k$Hz], and with a frequency increment of 100 Hz in the frequency range [1 $k$Hz, 2 $k$Hz] to enable a more precise curve fitting in the high frequency range, as indicated in Fig. 3 (b). The number of cycles per frequency is 10 and the number of samples per cycle is at least 40 to ensure accurate representations of the AC voltage and current waveforms. The measuring time for one IS measurement is around 31.3 s.

TABLE II
COMPARISON OF TWO CONTROL STRATEGIES

| Control strategy | Number of control parameters | Control bandwidth | Controller type |
|---|---|---|---|
| Unified control | 2 ($K_{pi}$, $\omega_{z-pi}$) | $\omega_{inj-max} \leq min[\frac{1}{9}\omega_{ct}, \omega_{inj-max-sys}]$ | PI controller |
| Separated control | 4 ($K_p$, $K_{pi-dc}$, $\omega_{z-pi-dc}$, $\omega_{0-LPF}$) | $\omega_{inj-max} \leq min[\frac{1}{9}\omega_{ct}, \omega_{inj-max-sys}]$ | PI + P controllers |
| | 7 ($K_{qpr}$, $K_r$, $\omega_{res-qpr}$, $\omega_{c-qpr}$, $K_{pi-dc}$, $\omega_{z-pi-dc}$, $\omega_{0-LPF}$) | $\omega_{inj-max} < \omega_{sw}$ | PI + QPR controllers |

TABLE III
CIRCUIT AND CONTROLLER PARAMETERS

| Description | Variables | Value |
|---|---|---|
| PV panel | Open-circuit voltage | $V_{oc}$ = 39.6 V |
| | Short-circuit current | $I_{sc}$ = 9.95 A |
| | Voltage at MPP | $V_{MPP}$ = 32.3 V |
| | Current at MPP | $I_{MPP}$ = 9.56 A |
| | Standard irradiance | $G$ = 1000 $W/m^2$ |
| | Standard temperature | $T$ = 25 $^oC$ |
| | Cells | 60 |
| | Cell surface | 156×156 $mm^2$ |
| Boost converter | Inductor | $L$ = 2.5 mH |
| | DC bus capacitor | $C$ = 260 $u$F |
| | Load | $R_L$ = 96 Ω |
| Operating information | Switching frequency | $f_{sw}$ = 80 $k$Hz |
| | Sampling frequency | $f_{sam-max}$ = 80 $k$Hz |
| | Perturbation signal frequency | $1e^{-3} \leq f_{inj} \leq 2$ $k$Hz |

### A. Comparison of the two control strategies

To compare the performance of the two control strategies based on the three compensation controllers, a set of experiments is conducted based on the configured parameters given in Section III. The experimental waveforms of PV panel voltage and current during IS implementation based on the three controllers are shown in Fig. 16. To evaluate the tracking performance of perturbation signals, three comparison criteria are defined:

$$Acc_{dc} = 1 - (I_{ref-dc} - I_{dc})/I_{ref-dc}$$

$$Acc_{Am} = 1 - MAPE_{Am} = 1 - \frac{1}{n}\sum_{\omega=\omega_1}^{\omega_n} \frac{Am_{\omega_i} - \hat{Am}_{\omega_i}}{Am_{\omega_i}}$$

$$SNR_{av} = \frac{1}{n}\sum_{\omega=\omega_1}^{\omega_n}(SNR_{\omega_i}) = \frac{1}{n}\sum_{\omega=\omega_1}^{\omega_n}(10log_{10}\frac{P_{signal_{\omega_i}}}{P_{noise_{\omega_i}}})$$

where $Acc_{dc}$ represents the tracking accuracy of DC component at the injection point, $Acc_{Am}$ represents the average amplitude tracking accuracy, $MAPE_{Am}$ represents the mean absolute percent error between the reference amplitude and the actual amplitude of the perturbation signal for each perturbation frequency $(\omega_1, \omega_2, ..., \omega_n)$. $SNR_{av}$ represents the average value of the SNR for each perturbation frequency (i.e., $SNR_{\omega_i}$), and $SNR_{\omega_i}$ is defined as the ratio in decibels of the summed squared magnitude of the perturbation signal (i.e., $P_{signal_{\omega_i}}$) to that of the noise (i.e., $P_{noise_{\omega_i}}$) at the perturbation frequency $\omega_i$. The tracking performance of the perturbation current signal in the frequency range of [1 Hz, 2 $k$Hz] are calculated and summarized in Table IV.

TABLE IV
TRACKING PERFORMANCE OF THREE CONTROLLERS

| Controller type | DC signal | AC signal | |
|---|---|---|---|
| | $Acc_{dc}$ | $Acc_{Am}$ | $SNR_{av}$ |
| PI | 99.5% | 93.7% | 6.9 dB |
| PI + P | 98.8% | 94.2% | 7.7 dB |
| PI + QPR | 99.2% | 96.5% | 5.2 dB |

The DC component tracking accuracies of the three controllers exceed 98%, indicating that all of them can effectively control the operation of the PV panel at the target injection point. Meanwhile, the results demonstrate that all three controllers are capable of tracking the perturbation current signal with a high accuracy ($> 90\%$). The values of SNR exceed 4.77 dB, which indicates that the power of the perturbation signal is at least three times greater than that of the noise (i.e., $10log_{10}$ (3) ≈ 4.77 dB), allowing for reliable extraction of the perturbation signal. In terms of AC component tracking accuracy, the QPR controller exhibits superior accuracy (i.e., 96.5%) as its control parameters are tuned in each divided frequency range. In terms of the SNR, the P controller has the biggest SNR (i.e., 7.7 dB). However, their control complexity is relatively higher than the single PI controller in terms of the number of control parameters.

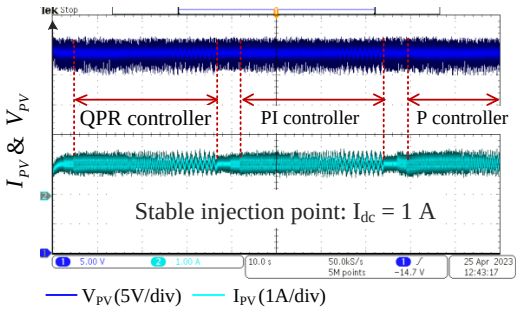


Fig. 16. Experimental waveforms of PV panel current and voltage with different controllers

According to the experimental results, the corresponding IS measurements of the PV panel based on the three controllers

are plotted in Fig. 17. It should be noted that in order to ensure the validity criteria, the IS measurements based on each controller are repeated at least five times. In the Bode plots, the asterisks represent the original values calculated from the experimental data, with grey, light blue and pink colors corresponding to the original IS measurements based on the P, PI and QPR controllers, respectively. The monochrome filled intervals are the corresponding confident intervals (i.e., 95%). The IS measurements calculated from the average value of amplitude and phase are shown as the solid line (blue, black and red separately) in Fig. 17 (a). The validity of IS measurements is further verified by passing the Kramers-Kronig (K-K) test based on an open source EIS analyzer [36]. In this test, all of the residuals (residuals of the real part $\Delta Re(\omega)$ and the imaginary part $\Delta Im(\omega)$) are less than 1%.

As shown in Fig. 17 (b), a good consistency of IS meaurements based on the three controllers can be observed. The root mean square error (RMSE) between the three IS curves depicted as the solid lines are less than 4.4%. It means that once the control parameters are appropriately set, all three controllers can achieve reliable and accurate IS measurements.

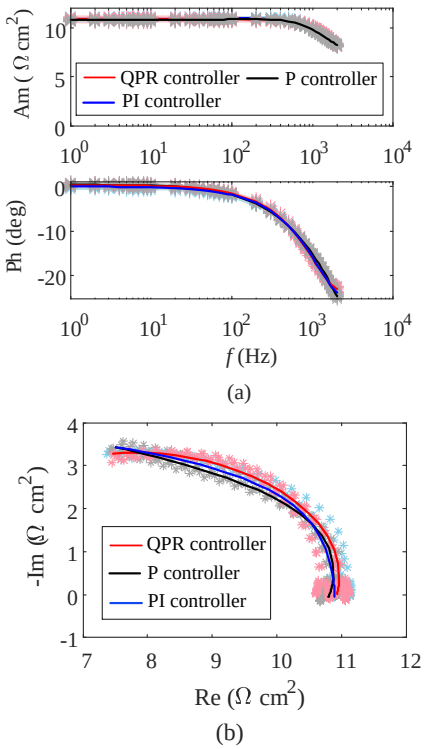


Fig. 17. Impedance information under different controllers: (a) Bode plots (b) Nyquist plots

As summarized in Table II, the unified control strategy based on a single PI controller has the least control parameters, while its tracking performance is comparable to that of separated control strategy based on the P/QPR controller. Considering the simplicity of the controller design, the high tracking accuracy ($> 90\%$) and sufficient SNR ($> 4.77$ dB), the PI controller based unified control strategy is further chosen for converter-based online IS implementation.

### B. Cooperative control of MPPT and IS modes

Under a constant irradiance ($G_1 = 250W/m^2$) and $T$ = 57 $^oC$, both I-V and P-V curves are measured for illustration, as shown in Fig. 18. As the PV output voltage varies, the MPP of the PV panel in the laboratory can reach 41 $W$ (power limited by the solar irradiance simulator), with the PV output current equal to 1.22 A at the MPP. The point at 1.0 A is selected as the injection point for the perturbation current signal to satisfy the linearity criterion, while ensuring quasi-maximum output power during IS mode. As aforementioned, the amplitude of the perturbation signal is set as 0.15 A, i.e., 15% of the DC component. It should be noted that the selection of this injection point is related to the type of the target PV panel and can be determined by analysing the I-V curves under the tested operating conditions.

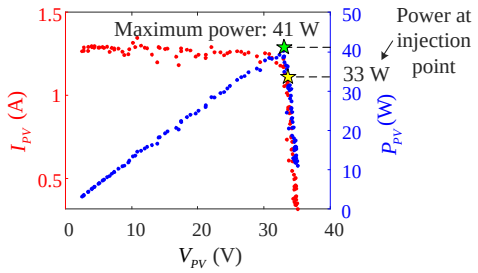


Fig. 18. Experimental waveform of I-V (red) and P-V curves (blue)

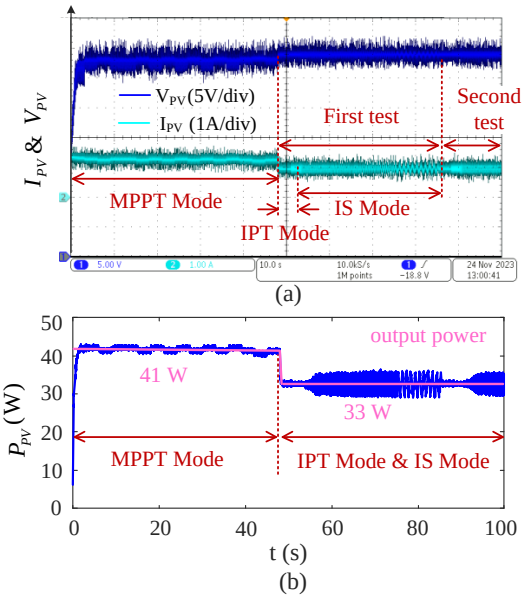


Fig. 19. Experimental waveform of the cooperative control between MPPT and IS modes: (a) output voltage and current (b) output power

An experimental test of the cooperative operation between MPPT and IS modes is performed and indicated in Fig. 19, with Fig. 19 (a) the PV output voltage and current and Fig. 19 (b) the PV output power. It can be observed that the PV panel operates initially in MPPT mode and then transitions to IS mode through IPT mode. The IPT mode takes around 3s for stabilization. To ensure the validity and

accuracy of IS measurements, multiple tests are repeated, with each including both IPT and IS modes, as illustrated in Fig. 2. From MPPT to IS mode, PV panel consistently produces power, and still maintain 80.5% of maximum output power. This power percentage can be even higher for larger-power panels since the PV current shifts slightly downward into quasi-linear voltage source region while the PV output voltage is quasi-constant in this region.

### C. IS measurements under different irradiance levels

To verify the effectiveness of the online IS monitoring, a series of initial experimental tests are performed under different irridiance levels, with the temperature of PV panel maintained. The mean values of IS measurements with at least five repetitions under each irridiance level are calculated and plotted in Fig. 20. It can be observed that the impedance curves shrink towards the lower left as the irradiance increases. The five tested irradiance levels are: $G_1 = 250W/m^2$, $G_2 = 263W/m^2$, $G_3 = 268W/m^2$, $G_4 = 284W/m^2$. $G_5 = 291W/m^2$.

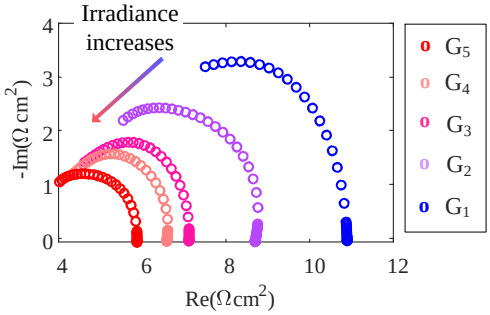


Fig. 20. Impedance information of different irradiance levels at the same injection point

Based on the acquired IS measurements, the corresponding equivalent circuit parameters indicated in Fig. 3 (c) are extracted and depicted in Fig. 21. As the irradiance increases, the value of $C_p$ increases, while $R_s$ and $R_p$ decrease. It can be verified that the change of the operating states of the PV panel can be reflected in real time through the evolution of internal impedance. A more detailed experimental study of IS measurements under more operating conditions such as different operating temperatures, different operating points, and different partial shading positions and areas have also been conducted. As the major focus of this work is on the control strategies of converter-based online IS, they are not shown herein, and are considered as the next-step work.

## V. Conclusions and Discussions

IS is an non-destructive tool that can obtain the PV panel's internal impedance in real time. The collaborative operation between MPPT and IS modes can improve the reliability of PV panels while ensuring (quasi-)maximum output power during the whole operating period. Unlike traditional IS implementation, which is generally based on a specific electrochemical workstation, the way based on existing power converters such as boost converters can greatly facilitate online health

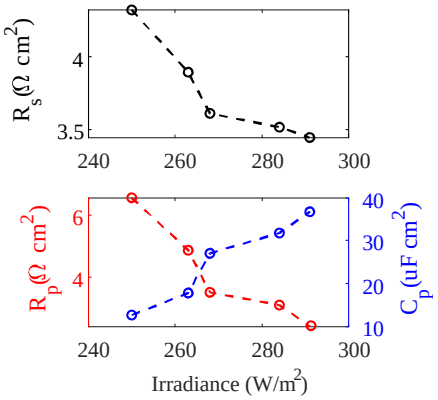


Fig. 21. Parameters of equivalent circuit model under different irradiances

monitoring. The perturbation signal can be directly generated by regulating the switching signals of the power converter.

To ensure the linearity and stability of the system during IS implementation, closed-loop current control with compensation controllers is emphasized in this work. Specifically, three commonly used controllers (P, PI and QPR) in linear system control are applied. According to their distinct characteristics, two control strategies, named unified control and separated control, are designed. In the unified control strategy, a single PI controller controls the DC and AC components together to meet the control objectives. Meanwhile, in the separated control strategy, when the P or QPR controller is used, a segmented LPF with a variable cut-off frequency is designed to separate firstly the DC and AC components. An additional PI controller is combined to control the PV panel at a steady-state operating point.

Based on the theoretical analysis and the experimental study, both control strategies can achieve the required control objectives for converter-based IS implementation in terms of tracking accuracy, control bandwidth and control stability. The separated control strategy based on the QPR controller enables the widest control bandwidth for the perturbation signal, while has the biggest number of control parameters (i.e., seven). The unified control strategy utilizing a single PI controller can achieve the same control bandwidth as the separated control strategy based on the P controller, while has a simpler design with only two control parameters. Considering the simplicity of the controller design, the high tracking accuracy (i.e., 99.5% for DC component and 93.7% for AC component) and sufficient SNR (i.e., 6.9 dB), the PI controller based unified control strategy is considered suitable for converter-based online IS implementation. The effectiveness of the online IS monitoring is initially verified as well. As an illustration, equivalent circuit parameters under different irradiance levels are extracted from IS measurements and can reflect the real-time evolution of the internal impedance of the PV panel. The proposed design guidelines for both control strategies is expected to be generalized to the online health monitoring of PV panels and other energy systems as well, such as batteries and fuel cells. In the next step, both short-term and long-term experimental studies based on IS measurements under various operating conditions and fault states will be conducted. Fault

diagnosis methods based on IS measurements are also under development for online health monitoring of PV panels.

## REFERENCES


[1] X. Wang, Z. Zheng, M. Aillerie, A. De Bernardinis, J. P. Sawicki, M. C. Péra, and D. Hissel, "Cooperative Control of Online Impedance Spectroscopy Monitoring Method and Maximum Power Point Tracking Method for Photovoltaic Panels," in *24th European Conference on Power Electronics and Applications, EPE 2022 ECCE Europe*, 2022.

[2] H. M. Khalid, Z. Rafique, S. M. Muyeen, A. Raqeeb, Z. Said, R. Saidur, and K. Sopian, "Dust accumulation and aggregation on PV panels: An integrated survey on impacts, mathematical models, cleaning mechanisms, and possible sustainable solution," *Solar Energy*, vol. 251, no. July 2022, pp. 261–285, 2023. [Online]. Available: https://doi.org/10.1016/j.solener.2023.01.010

[3] A. Aldosary, Z. M. Ali, M. M. Alhaider, M. Ghahremani, S. Dadfar, and K. Suzuki, "A modified shuffled frog algorithm to improve MPPT controller in PV System with storage batteries under variable atmospheric conditions," *Control Engineering Practice*, vol. 112, no. February 2020, p. 104831, 2021. [Online]. Available: https://doi.org/10.1016/j.conengprac.2021.104831

[4] S. Ali, Z. Zheng, M. Aillerie, J. P. Sawicki, M. C. Péra, and D. Hissel, "A review of dc microgrid energy management systems dedicated to residential applications," *Energies*, vol. 14, no. 14, pp. 1–26, 2021.

[5] D. A. R. Barkhouse, O. Gunawan, T. Gokmen, T. K. Todorov, and D. B. Mitzi, "On the detection of shunts in silicon solar cells by photo and electroluminescence imaging," *Progress in Photovoltaics: Research and Applications*, vol. 20, no. 1, pp. 6–11, 2015. [Online]. Available: http://dx.doi.org/10.1002/pip.1160

[6] G. M. El-Banby, N. M. Moawad, B. A. Abouzalm, W. F. Abouzaid, and E. A. Ramadan, "Photovoltaic system fault detection techniques: a review," *Neural Computing and Applications*, vol. 35, no. 35, pp. 24 829–24 842, 2023. [Online]. Available: https://doi.org/10.1007/s00521-023-09041-7

[7] R. Duru, D. Le Cunff, M. Cannac, I. Mica, J. Baruchel, T. N. Tran-Thi, and G. Bremond, "Photoluminescence Imaging for Buried Defects Detection in Silicon: Assessment and Use-Cases," *IEEE Transactions on Semiconductor Manufacturing*, vol. 32, no. 1, pp. 23–30, 2019.

[8] K. Bedrich, M. Bokalic, M. Bliss, M. Topic, T. R. Betts, and R. Gottschalg, "Electroluminescence Imaging of PV Devices: Advanced Vignetting Calibration," *IEEE Journal of Photovoltaics*, vol. 8, no. 5, pp. 1297–1304, 2018.

[9] K. G. Bedrich, W. Luo, M. Pravettoni, D. Chen, Y. Chen, Z. Wang, P. J. Verlinden, P. Hacke, Z. Feng, J. Chai, Y. Wang, A. G. Aberle, and Y. S. Khoo, "Quantitative Electroluminescence Imaging Analysis for Performance Estimation of PID-Influenced PV Modules," *IEEE Journal of Photovoltaics*, vol. 8, no. 5, pp. 1281–1288, 2018.

[10] Jahn Ulrike, Herz Magnus, Köntges Marc, Parlevliet David, Paggi Marco, and Tsanakas Ioannis, "Review on infrared and electroluminescence imaging for PV field applications," Tech. Rep., 2018. [Online]. Available: https://iea-pvps.org/key-topics/review-on-ir-and-el-imaging-for-pv-field-applications/

[11] S. Fadhel, C. Delpha, D. Diallo, I. Bahri, A. Migan, M. Trabelsi, and M. F. Mimouni, "PV shading fault detection and classification based on I-V curve using principal component analysis: Application to isolated PV system," *Solar Energy*, vol. 179, pp. 1–10, 2019.

[12] M. Ma, Z. Zhang, P. Yun, Z. Xie, H. Wang, and W. Ma, "Photovoltaic module current mismatch fault diagnosis based on I-V Data," *IEEE Journal of Photovoltaics*, vol. 11, no. 3, pp. 779–788, 2021.

[13] B. Li, C. Delpha, A. Migan-Dubois, and D. Diallo, "Fault diagnosis of photovoltaic panels using full I–V characteristics and machine learning techniques," *Energy Conversion and Management*, vol. 248, p. 114785, 2021. [Online]. Available: https://doi.org/10.1016/j.enconman.2021.114785

[14] M. K. Alam, F. H. Khan, J. Johnson, and J. Flicker, "PV arc-fault detection using spread spectrum time domain reflectometry (SSTDR)," *2014 IEEE Energy Conversion Congress and Exposition, ECCE 2014*, pp. 3294–3300, 2014.

[15] S. R. Madeti and S. N. Singh, "A comprehensive study on different types of faults and detection techniques for solar photovoltaic system," *Solar Energy*, vol. 158, no. June, pp. 161–185, 2017. [Online]. Available: https://doi.org/10.1016/j.solener.2017.08.069

[16] M. A. Varnosfaderani and D. Strickland, "Online Electrochemical Impedance Spectroscopy (EIS) estimation of a solar panel," *Vacuum*, vol. 139, pp. 185–195, 2017. [Online]. Available: http://dx.doi.org/10.1016/j.vacuum.2017.01.011

[17] J. A. A. Qahouq, S. Member, Z. Xia, and S. Member, "Single-Perturbation-Cycle Online Battery Impedance Spectrum Measurement Method With Closed-Loop Control of Power Converter," *IEEE Transactions on Industrial Electronics*, vol. 64, no. 9, pp. 7019–7029, 2017.

[18] H. H. Abbasali and S. Jafarabadi Ashtiani, "Online Broadband Battery Impedance Spectroscopy Using Current-Mode Boost Converter," *IEEE Transactions on Instrumentation and Measurement*, vol. 71, pp. 1–8, 2022.

[19] O. I. Olayiwola and P. S. Barendse, "Power Electronic Implementation of Electrochemical Impedance Spectroscopy on Photovoltaic Modules," *ECCE 2020 - IEEE Energy Conversion Congress and Exposition*, pp. 3654–3661, 2020.

[20] S. Moore and P. Barendse, "Online condition monitoring of lithium-ion batteries using impedance spectroscopy," *2017 IEEE Energy Conversion Congress and Exposition, ECCE 2017*, vol. 2017-Janua, pp. 5617–5624, 2017.

[21] T. T. Nguyen, V. T. Doan, and W. Choi, "Design of a fuel cell power conditioning system for online diagnosis and load leveling," *Journal of Power Electronics*, vol. 16, no. 2, pp. 695–703, 2016.

[22] S. M. Islam and S. Y. Park, "Precise Online Electrochemical Impedance Spectroscopy Strategies for Li-Ion Batteries," *IEEE Transactions on Industry Applications*, vol. 56, no. 2, pp. 1661–1669, 2020.

[23] E. Von Hauff, "Impedance Spectroscopy for Emerging Photovoltaics," *Journal of Physical Chemistry C*, vol. 123, no. 18, pp. 11 329–11 346, 2019.

[24] T. Tanahashi, N. Sakamoto, H. Shibata, and A. Masuda, "Localization and characterization of a degraded site in crystalline silicon photovoltaic cells exposed to acetic acid vapor," *IEEE Journal of Photovoltaics*, vol. 8, no. 4, pp. 997–1004, 2018.

[25] W. Huang and J. A. Qahouq, "An online battery impedance measurement method using DC-DC power converter control," *IEEE Transactions on Industrial Electronics*, vol. 61, no. 11, pp. 5987–5995, 2014.

[26] X. Wang, Z. Zheng, M. Aillerie, A. De Bernardinis, M.-C. Péra, and D. Hissel, "Online Impedance Spectroscopy Characterization of PV Panels by Studying Resonant Behavior of Boost Converter," in *2023 IEEE Transportation Electrification Conference & Expo (ITEC)*, 2023, pp. 1–7.

[27] Q. Guo, I. Bahri, D. Diallo, and E. Berthelot, "Model predictive control and linear control of DC–DC boost converter in low voltage DC microgrid: An experimental comparative study," *Control Engineering Practice*, vol. 131, no. October 2022, p. 105387, 2023. [Online]. Available: https://doi.org/10.1016/j.conengprac.2022.105387

[28] J. Shen, H. Homayouni, and J. Wang, "Converter-Based Electrochemical Impedance Spectroscopy for High-Power Fuel Cell Stacks with Resonant Controllers," *IEEE Transactions on Industrial Electronics*, vol. 68, no. 9, pp. 8819–8828, 2021.

[29] L. Shelembe and P. Barendse, "An Adaptive Amplitude-Modulated Pseudo-Random Binary Sequence Excitation for Converter-Based Impedance Spectroscopy Characterization of Photovoltaic Modules," *IEEE Transactions on Industry Applications*, vol. 59, no. 2, pp. 2007–2018, 2023.

[30] Z. Zheng, X. Wang, and Y. Li, "A control method for grid-friendly photovoltaic systems with hybrid energy storage units," *DRPT 2011 - 2011 4th International Conference on Electric Utility Deregulation and Restructuring and Power Technologies*, no. 51007044, pp. 1437–1440, 2011.

[31] M. W. Losey and J. J. Kelly, *Electrochemical Impedance Spectroscopy and its Applications*. New York, USA: Springer Science+Business Media New York, 2014, vol. 1.

[32] X. Yuan, J. C. Sun, M. Blanco, H. Wang, J. Zhang, and D. P. Wilkinson, "AC impedance diagnosis of a 500 W PEM fuel cell stack. Part I: Stack impedance," *Journal of Power Sources*, vol. 161, no. 2, pp. 920–928, 2006.

[33] Z. Zheng, R. Petrone, M. C. Pera, D. Hissel, M. Becherif, and C. Pianese, "Diagnosis of a commercial PEM fuel cell stack via incomplete spectra and fuzzy clustering," *IECON 2013 - 39th Annual Conference of the IEEE Industrial Electronics Society*, pp. 1595–1600, 2013.

[34] E. R. da Silva and M. E. Elbuluk, *Fundamentals of Power Electronics*. Cham, Switzerland:Springer Nature Switzerland AG: Springer, 2013, vol. 59.

[35] T. Ye, N. Y. Dai, C. S. Lam, M. C. Wong, and J. M. Guerrero, "Analysis, design, and implementation of a quasi-proportional-resonant controller for a multifunctional capacitive-coupling grid-connected inverter," *IEEE Transactions on Industry Applications*, vol. 52, no. 5, pp. 4269–4280, 2016.

[36] A. Bandarenka and G. Ragoisha, "EIS Spectrum Analyser," 2008. [Online]. Available: http://www.abc.chemistry.bsu.by/vi/analyser